Check for updates

Angewandte Chemie International Edition

Angewandte International Edition Chemie

How to cite: *Angew. Chem. Int. Ed.* **2026**, 65, e2842007
doi.org/10.1002/anie.2842007

RESEARCH ARTICLE

Tuning Local Charge-Density in COFs to Suppress Protonation and Unlock Binding Sites for Efficient Palladium Recovery

Shijie Xiong[1] | Pei Chen[1] | Hanzhi Chen[1] | Muliang Xiao[1] | Ruining Cao[1] | Jiaqi Li[1] | Chuanlei Luo[1] | Xinyi Yang[1] | Xiaolu Liu[1] | Yinghui Xie[1] | Mengjie Hao[1] | Geoffrey I. N. Waterhouse[2] | Xiangke Wang[1] | Shengqian Ma[3] | Hui Yang[1]

[1]College of Environmental Science and Engineering, North China Electric Power University, Beijing, China | [2]School of Chemical Sciences, The University of Auckland, Auckland, New Zealand | [3]Department of Chemistry, University of North Texas, Denton, USA

Correspondence: Xiangke Wang (xkwang@ncepu.edu.cn) | Shengqian Ma (shengqian.ma@unt.edu) | Hui Yang (h.yang@ncepu.edu.cn)

Received: 6 March 2026 | **Revised:** 24 May 2026 | **Accepted:** 28 May 2026

Keywords: charge density | covalent organic frameworks | Pd(II) recovery | selective adsorption | suppress protonation

ABSTRACT

Imine-linked COFs are increasingly being used to recover palladium from aqueous waste streams, but the binding sites undergo protonation in acidic media, thereby losing palladium adsorption capacity. Herein, we report a new strategy that effectively suppresses imine protonation in COFs by tuning the local charge density, thereby allowing highly efficient recovery of Pd(II) from acidic solutions. By judicious placement of electron-donating hydroxyl substituents on aromatic units next to imine groups, the electron cloud density around imine N atoms increases, suppressing protonation and preserving a high density of accessible Pd(II) binding sites. Further incorporation of extended π-conjugated naphthalene units increases local charge density at the imine centers, strengthening the Pd(II) affinity and boosting adsorption capacity. As a result, the optimized adsorbent (COF-3) exhibits rapid adsorption kinetics, exceptional selectivity, and an unprecedented Pd(II) uptake of 942.02 ± 24.61 mg/g in 0.1 M HNO_3, surpassing all reported crystalline adsorbents thus far. Subsequently, COF-3 demonstrates robust performance in dynamic recovery of Pd(II) from both acidic laboratory waste streams and simulated high-level radioactive liquid waste, while maintaining excellent adsorption efficiency across multiple adsorption-desorption cycles. Our rational strategy opens a new avenue for designing next-generation sorbents for precious metal recovery and other applications.

1 | Introduction

Palladium (Pd) is an extremely scarce precious metal in the Earth's crust though plays an indispensable role in a wide range of applications [1], including automotive exhaust catalytic convertor systems [2], fine chemical catalysis [3, 4], electronic devices [1, 5], pharmaceutical synthesis [6, 7], and hydrogenation processes [8, 9]. With the rapid growth of these industries, global demand for palladium continues to rise, while its natural reserves are highly concentrated and its exploitable resources remain limited, leading to a growing supply-demand imbalance. Notably, Pd is widely present in secondary resources, including metallurgical wastewater [10, 11], spent catalysts [12, 13], waste electrical, and electronic equipment (WEEE) [14, 15], and high-level radioactive liquid waste (HLLW) generated during nuclear fuel reprocessing [16, 17]. Compared with primary ore mining and smelting, recovery

Shijie Xiong, Pei Chen, and Hanzhi Chen contributed equally to this work.

© 2026 Wiley-VCH GmbH

of palladium from secondary resources generally requires lower energy input and cost while reducing environmental burdens, making it both economically and environmentally attractive [1, 18]. Furthermore, Pd-containing wastes may be landfilled or improperly discharged without effective recovery, resulting in heavy metal migration into soil and water systems and causing long-term environmental risks [19, 20]. Therefore, developing efficient palladium recovery technologies from complex waste streams is of both strategic and environmental importance.

Whilst efficient recovery of palladium from waste streams has strategic importance, it remains highly challenging with palladium coexisting with numerous competing metal ions under high ionic strength conditions in most waste streams, placing stringent requirements on separation selectivity [21, 22]. Furthermore, palladium-containing waste (existing as Pd(II)) is generally dissolved in acid, typically nitric acid solutions, which complicates recovery. Under such conditions, Pd(II) capture predominantly relies on electron-donating coordination sites of stable sorbents to form strong metal-ligand interactions. A wide range of adsorbents, including inorganic materials [16, 23], porous organic polymers [24, 21], and metal-organic frameworks (MOFs) have been explored for selective Pd(II) capture [25, 26], generally relying on surface functional groups or lone-pair electrons to bind Pd(II) through coordination or electrostatic interactions. However, these sorbents exhibit performance degradation and even lose their binding activity when exposed to strongly acidic solutions [27]. This is because protonation or competitive occupation of coordination sites reduces the effective binding of Pd(II), whilst limited control over the spatial distribution and local microenvironment of adsorption sites further hinders efficient matching of the preferred coordination geometry of Pd(II) [24, 27]. Therefore, a number of reported adsorbents exhibit drawbacks such as slow adsorption kinetics, low adsorption capacity, poor selectivity, and/or short-term reusability when applied in acidic media [21, 28].

Recently, covalent organic frameworks (COFs), featuring ordered pore structures, programmable backbones, and high chemical stability, have provided a unique platform for precious metal recovery and separation [22, 29–32]. In particular, imine-linked COFs have been extensively investigated for Pd(II) capture due to their structural tunability and high surface area [27, 33–35]. However, imine-linked COFs suffer from a fundamental limitation under acidic conditions: The N atoms in imine bonds are readily protonated, which markedly weakens their metal coordination ability and renders a large fraction of potential active sites inactive. This protonation effect intensifies markedly in acidic solution, limiting the Pd(II) adsorption capacity and selectivity in waste streams. To address this issue, Bai and coworkers reported an imine-based COF functionalized with para-hydroxyl groups (*trans* C═N configuration), in which enol-keto tautomerism under acidic conditions generates interlayer carbonyl sites that allowed Pd(II) coordination (Figure 1a) [27]. This notable approach converts the hydroxyl groups on one side of the aromatic ring to an enol-ketone structure, while hydroxyl groups on the opposite side remain in their enol form. However, the imine N atoms within individual layers remain highly susceptible to protonation under acidic conditions. As a result, both the non-tautomerized hydroxyl groups and the protonated imine N atoms are ineffective at coordinating to Pd(II), leading to intrinsically incomplete utilization of available binding sites. Moreover, the extent of asymmetric tautomerization, along with the generation of effective binding sites is strongly influenced by interlayer distance and proton-transfer pathways, making the universal activation of binding sites difficult to achieve. Thus, a substantial fraction of intrinsic framework functionalities remains inaccessible to bind Pd(II) in acidic solutions, underscoring the need for further exploration.

Inspired by the aforementioned studies, we herein propose a new strategy to suppress imine nitrogen protonation by deliberately tuning the local charge density around N atoms in imine-linked COFs, thereby preserving and activating intrinsic N sites under acidic conditions and enabling synergistic coordination of Pd(II) via nearby O sites (Figure 1b). Unlike conventional strategies that primarily incorporate functional groups, this approach increased the electron cloud density around imine N atoms, thereby reducing their susceptibility to proton attack in acidic solutions. Specifically, electron-donating hydroxyl groups are strategically positioned on the same side of the aromatic rings to increase localized electron density, thereby weakening the protonation tendency of imine N atoms (*cis* C═N configuration) and increasing N-site availability for Pd(II) binding (Figure 1b, c). Subsequently, benzene units were substituted with naphthalene units to enhance the synergistic effects of N—OH sites, yielding a framework (denoted as COF-3) with increased local charge density. This approach not only further suppresses nitrogen protonation, but also strengthens Pd(II)-framework interactions (Figure 1b, c). As a result, COF-3 with the highest local charge density achieves fast adsorption kinetics, excellent selectivity, and an exceptional Pd(II) adsorption capacity of 942.02 ± 24.61 mg/g in 0.1 M HNO_3. COF-2 with hydroxyl substituents on the same side of the aromatic units (forming a *cis* C═N configuration), featuring a relatively lower local charge density, exhibits correspondingly reduced adsorption performance. Nevertheless, it remains higher than that of COF-1 (with para-hydroxyl groups forming the *trans* C═N configuration). Moreover, COF-3 can dynamically and efficiently capture Pd(II) from lab-generated Pd-containing waste and simulated acidic HLLW solutions, while maintaining stable performance across multiple adsorption-desorption cycles. These results provide a new design strategy for high-performance adsorbents targeting selective palladium recovery from complex acidic waste streams.

2 | Results and Discussion

2.1 | COFs Synthesis and Characterization

To address the protonation-induced deactivation of imine N sites in COFs under acidic conditions, a family of imine-linked COFs was designed and synthesized by varying the relative positions of hydroxyl groups and extending the π-conjugation of the aldehyde building blocks. As shown in Figure 1c, COF-1, COF-2, and COF-3 were synthesized via Schiff-base condensation of 4,4',4'',4'''-([9,9'-Bicarbazole]-3,3',6,6'-tetrayl)tetraaniline (BCTA) with 2,5-dihydroxy-1,4-benzenedicarboxaldehyde (DA), 2,3-dihydroxyterephthalaldehyde (DB), or 2,3-dihydroxynaphthalene-1,4-dicarbaldehyde (DHD) in 1,2-dichlorobenzene (o-DCB)/N,N-dimethylacetamide (DMAc)/acetic acid (AcOH) (5:5:1, v/v/v) at 120 °C for three

15213773, 2026, 33, Downloaded from https://onlinelibrary.wiley.com/doi/10.1002/anie.202402007 by Shengqian Ma - University Of North Texas Willis Library , Wiley Online Library on [21/10/2026]. See the Terms and Conditions (https://onlinelibrary.wiley.com/terms-and-conditions) on Wiley Online Library for rules of use; OA articles are governed by the applicable Creative Commons License

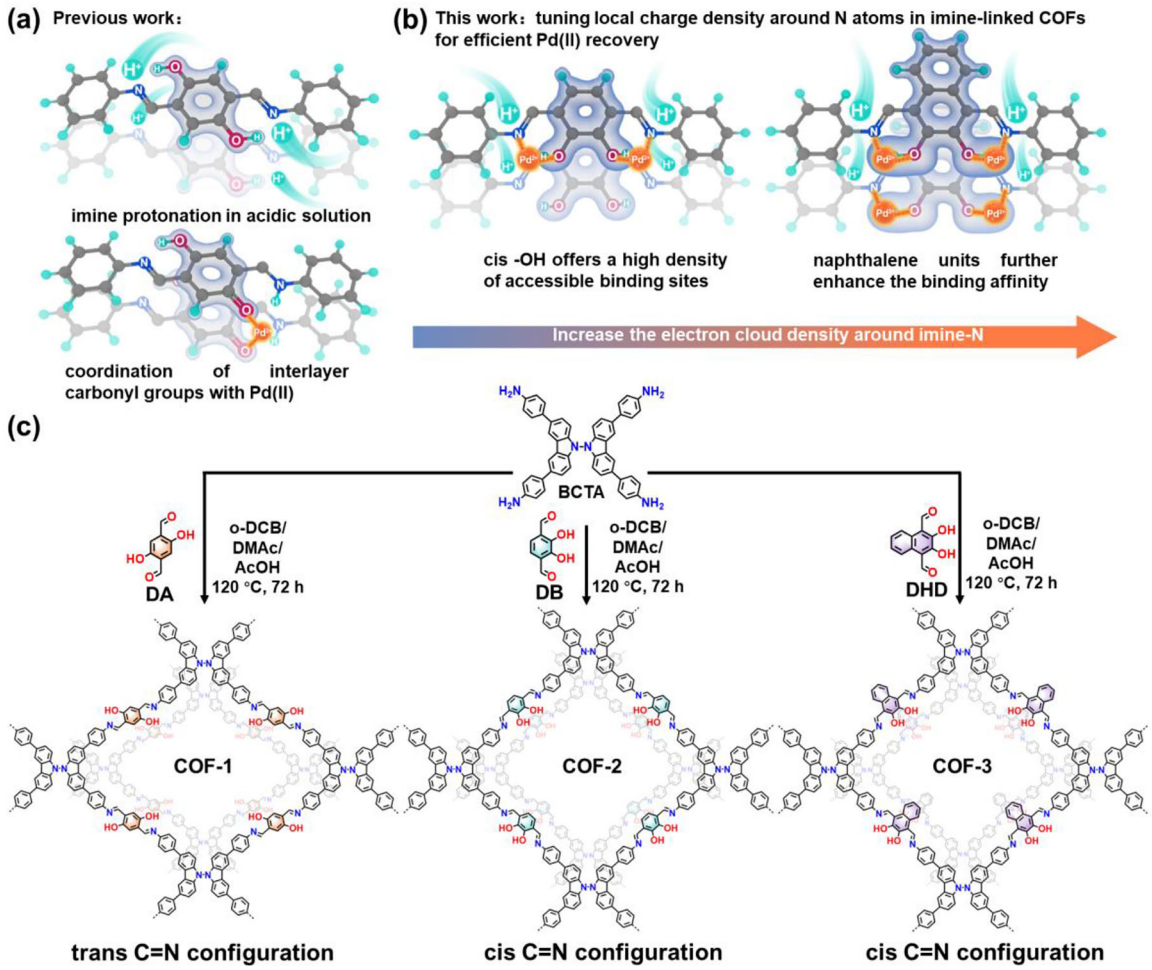


FIGURE 1 | (a) Schematic illustration of an imine-based COF functionalized with para-hydroxyl groups, in which enol-keto tautomerism under acidic conditions generates interlayer carbonyl sites that allow Pd(II) coordination. (b) The strategy to suppress imine nitrogen protonation by deliberately tuning the local charge density around N atoms in imine-linked COFs (showing significantly enhanced utilization and affinity of Pd(II) binding sites). (c) Illustration of the synthesis of COF-1, COF-2, and COF-3.

days. The formation of imine-linked frameworks was first confirmed by Fourier transform infrared (FT-IR) spectroscopy and solid-state ^{13}C cross-polarization magic angle spinning nuclear magnetic resonance (^{13}C CP/MAS NMR) spectroscopy. In the FT-IR spectra (Figures 2a, S1), characteristic C═N stretching vibrations appeared at 1613, 1616, and 1620 cm^{-1} for COF-1, COF-2, and COF-3, respectively, accompanied by the complete disappearance of aldehyde C═O bands from the corresponding monomers (DA: 1670 cm^{-1}, DB: 1655 cm^{-1}, DHD: 1647 cm^{-1}), indicating successful condensation [36–39]. The ^{13}C CP/MAS NMR spectra further displayed distinct resonances at 161.5, 161.2, and 158.3 ppm, characteristic of imine carbon atoms, while additional signals at 139.1, 139.7, and 138.5 ppm were assigned to phenolic carbons in DA-, DB-, and DHD-derived linkers, further verifying framework formation (Figure 2b) [36–38]. Next, the crystalline structures of the three COFs were investigated by powder X-ray diffraction (PXRD) and by structural simulations using Materials Studio software. COF-1 exhibited prominent diffraction peaks at $2\theta = 3.45°$ and 6.90°, which could be indexed to the (110) and (220) planes, respectively (Figures 2c, S2). Pawley refinement indicated that COF-1 crystallizes in the C2 space group with lattice parameters $a = 35.04$ Å, $b = 43.21$ Å, $c = 4.23$ Å, $\alpha = 90.00°$, $\beta = 123.21°$, $\gamma = 90.00°$, affording low residual factors ($R_p = 2.73\%$, $R_{wp} = 3.60\%$) (Table S1). The experimental pattern agreed well with a simulated eclipsed AA stacking model, yielding a calculated interlayer distance of ~4.2 Å and a pore diameter of ~1.9 nm, respectively (Figure 2d, Table S1). Similarly, COF-2 displayed diffraction peaks at $2\theta = 3.38°$, 4.76°, 6.72°, and 10.18°, corresponding to the (110), (210), (220), and (400) planes, respectively. Pawley refinement revealed a C2 space group with lattice parameters $a = 43.73$ Å, $b = 34.13$ Å, $c = 4.00$ Å, $\alpha = \beta = \gamma = 90.00°$ ($R_p = 1.45\%$, $R_{wp} = 1.94\%$), consistent with a *cis*-eclipsed AA (*cis*-AA) stacking mode constructed by using Materials Studio software (Figures 2e, S3, and Table S2). The calculated interlayer spacing and pore size were ~4.0 Å and ~2.1 nm, respectively (Figure 2f). COF-3 showed characteristic PXRD reflections at $2\theta = 3.45°$, 5.07°, and 6.89°, corresponding to the (110), (210), and (220) planes. Structural refinement confirmed a C2 symmetry with lattice parameter $a = 33.68$ Å, $b = 42.76$ Å, $c = 4.17$ Å, $\alpha = 90.00°$, $\beta = 103.96°$, $\gamma = 90.00°$ ($R_p = 2.65\%$, $R_{wp} = 3.65\%$), in good agreement with a *cis*-AA stacking model (Figures 2g, S4, and Table S3). The

15213773, 2026, 33, Downloaded from https://onlinelibrary.wiley.com/doi/10.1002/anie.202412007 by Shengqian Ma - University Of North Texas Willis Library , Wiley Online Library on [21/10/2026]. See the Terms and Conditions (https://onlinelibrary.wiley.com/terms-and-conditions) on Wiley Online Library for rules of use; OA articles are governed by the applicable Creative Commons License

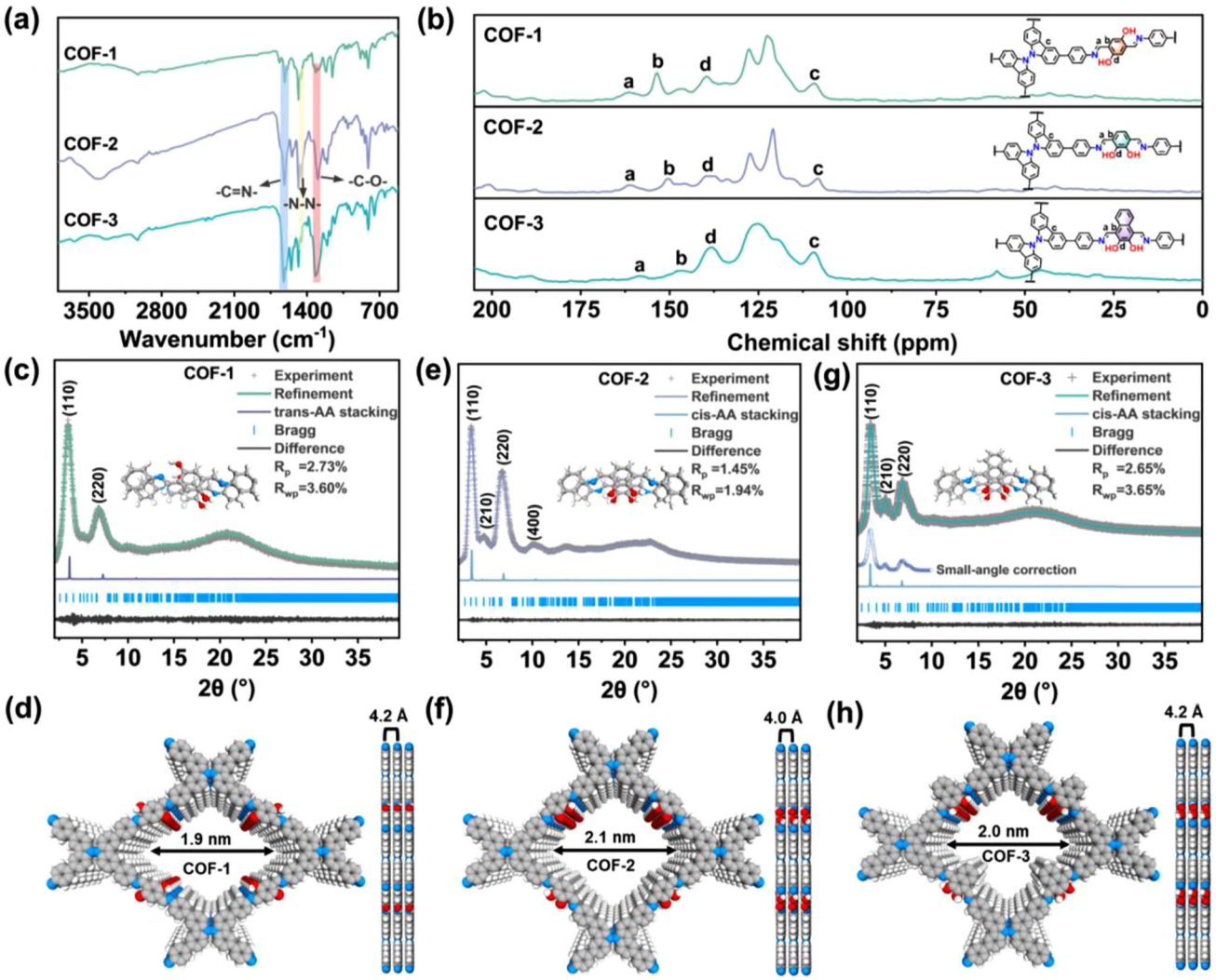


FIGURE 2 | (a) FT-IR spectra of COF-1, COF-2, and COF-3. (b) ^{13}C CP/MAS solid-state NMR spectra of COF-1, COF-2, and COF-3. (c) Experimental PXRD patterns of COF-1 with corresponding Pawley refinement (light green), simulated results (purple), and Bragg positions (blue) showing good fits to the experimental data (light gray) with minimal differences (dark gray). (d) Top and side views of the AA stacking crystal structures of COF-1. (e) Experimental PXRD patterns of COF-2 with corresponding Pawley refinement (light purple), simulated results (light blue), and Bragg positions (blue) showing good fits to the experimental data (light gray) with minimal differences (dark gray). (f) Top and side views of the AA stacking crystal structures of COF-2. (g) Experimental PXRD patterns of COF-3 with corresponding Pawley refinement (light cyan), simulated results (light blue), and Bragg positions (blue) showing good fits to the experimental data (light gray) with minimal differences (dark gray). SAXS data were used for zero-shift correction. (h) Top and side views of the AA stacking crystal structures of COF-3.

simulated interlayer distance and pore diameter were estimated to be ~4.2 Å and ~2.0 nm, respectively (Figure 2h). High-resolution transmission electron microscopy (HR-TEM) further showed well-defined lattice fringes with spacings of ~2.1 and ~2.0 nm for COF-2 and COF-3, respectively, consistent with the PXRD simulation results (Figure 3a, b). To further probe the stacking structures of COF-2 and COF-3, we built other possible models by arranging linkers in eclipsed AA stacking and staggered AB stacking configurations (Figures S3, S4). In contrast, the simulated PXRD pattern of COF-2 with an eclipsed *trans*-AA stacking mode displayed a distinct diffraction peak at $2\theta = 11.05°$, which is absent in the experimental PXRD pattern. Similarly, the simulated eclipsed *trans*-AA model for COF-3 failed to reproduce the pronounced diffraction feature observed experimentally at around $2\theta = 5.07°$. Moreover, staggered AB stacking configurations could be excluded by comparing experimental and simulated PXRD patterns in the 2θ range of approximately 2–15°, where clear mismatches were observed. In contrast, the simulated PXRD patterns based on a *cis*-AA stacking model showed excellent agreement with the experimental data for both COF-2 and COF-3, supporting the assignment of a parallel *cis*-AA stacking arrangement. Small-angle X-ray scattering (SAXS) pattern further confirmed the *cis*-AA stacking structure of COF-3 (Figure 2g). The preferential adoption of *cis*-AA stacking in COF-2 and COF-3 is attributed to interlayer hydrogen bonding interactions (O—H···N) involving imine nitrogen atoms and hydroxyl-functionalized linkers, which stabilize parallel stacking arrangements [40].

Nitrogen adsorption-desorption data measured at 77 K revealed Type II isotherms for all three COFs (Figure 3c). The Brunauer-Emmett-Teller (BET) surface areas were determined to be 766.3,

15213773, 2026, 33, Downloaded from https://onlinelibrary.wiley.com/doi/10.1002/anie.202402007 by Shengqian Ma - University Of North Texas Willis Library , Wiley Online Library on [21/10/2026]. See the Terms and Conditions (https://onlinelibrary.wiley.com/terms-and-conditions) on Wiley Online Library for rules of use; OA articles are governed by the applicable Creative Commons License

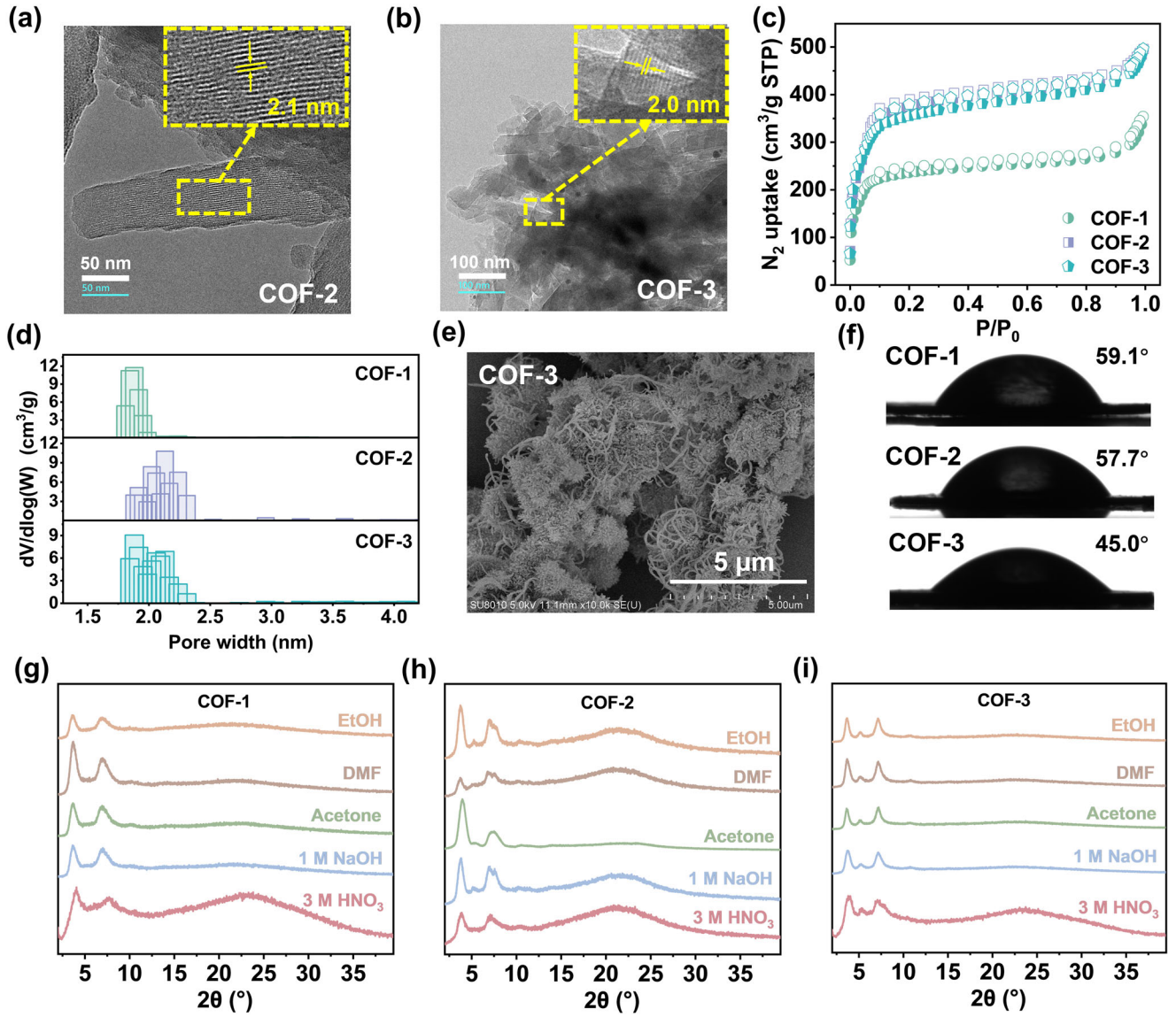


FIGURE 3 | (a, b) TEM images of COF-2 and COF-3. (c, d) N_2 sorption isotherms and pore size distributions measured at 77 K for COF-1, COF-2, and COF-3. (e) SEM image of COF-3. (f) Contact angle for a water droplet on pressed pellets of COF-1, COF-2, and COF-3. (g–i) PXRD patterns of COF-1, COF-2, and COF-3 after treatment under different conditions for 24 h.

1236.4, and 1169.3 m^2/g for COF-1, COF-2, and COF-3, respectively. Pore size distributions derived from functional theory (DFT) analysis gave pore diameters of ~1.9 (COF-1), ~2.1 (COF-2), and ~2.0 nm (COF-3), consistent with simulated structural models (Figure 3d). Scanning electron microscopy (SEM) images revealed that all three COFs possess interconnected fibrous morphologies (Figures 3e, S5, S6). The surface wettability of the COFs was evaluated by water contact angle measurements. Contact angles of 59.1°, 57.7°, and 45.0° were obtained for COF-1, COF-2, and COF-3, respectively, evidencing their mild hydrophilic properties (Figure 3f). Thermogravimetric analysis (TGA) under a nitrogen atmosphere showed that COF-1, COF-2, and COF-3 exhibited small mass losses below 150° C (due to desorption of water and solvent molecules), then negligible further mass losses until heated to temperatures above 450° C (Figure S7), indicating their good thermal stability. Subsequently, the chemical stabilities of the COFs were evaluated by immersing them in various solvents (Ethanol, EtOH; N,N-dimethylformamide, DMF; acetone) and in acid and alkaline solutions (3 M HNO_3 and 1 M NaOH, respectively). The samples treated under various conditions were further characterized by PXRD and nitrogen adsorption-desorption analysis. PXRD analysis showed only a very slight decrease in intensity after these treatments, indicating the crystalline frameworks remained intact (Figures 3g–i). N_2 adsorption-desorption isotherms and corresponding pore-size distribution analyses were subsequently performed to explore the porosities of the three COFs after chemical treatments (Figure S8). COF-1 and COF-2 showed obvious decreases in N_2 uptake after treatments with HNO_3 or NaOH, whereas COF-3 was much less affected, indicating better retention of accessible porosity. In terms of pore-size distributions, COF-1 showed minor changes after treatment with HNO_3 and NaOH, but exhibited a slight increase in average pore width following treatment with DMF. The slightly stretched pores of DMF-treated COF-1 may be related to solvent-assisted removal of residual guests/oligomers and pore-channel relaxation. In comparison, COF-2 showed almost

15213773, 2026, 33, Downloaded from https://onlinelibrary.wiley.com/doi/10.1002/anie.202402007 by Shengqian Ma - University Of North Texas Willis Library , Wiley Online Library on [21/10/2026]. See the Terms and Conditions (https://onlinelibrary.wiley.com/terms-and-conditions) on Wiley Online Library for rules of use; OA articles are governed by the applicable Creative Commons License

unchanged average pore width across all tested conditions. COF-3 retained its pore width after treatments with NaOH and DMF, but a modest narrowing was observed after treatment with HNO_3, likely attributable to framework contraction or interlayer stacking reorganization under strongly acidic conditions. Overall, the well-defined crystalline structures, high porosity, hydrophilic surfaces, and excellent chemical stability of the three COFs (particularly COF-3) establish a solid structural foundation for subsequent investigations of their Pd(II) adsorption performance under acidic conditions. To validate the utility of hydroxyl groups for enhanced Pd(II) adsorption, we also synthesized hydroxyl-free analogue frameworks (COF-4 and COF-5) by condensation of BCTA with terephthalaldehyde (TPDA) and naphthalene-1,4-dicarbaldehyde (NDA), respectively [36, 41]. The synthesis and characterization data for COF-4 and COF-5 are provided in the Figures S9–S12.

2.2 | Pd(II) Adsorption Studies

The Pd(II) adsorption performance of the synthesized COFs was systematically evaluated under acidic conditions to assess their suitability for palladium recovery from practical waste streams. Preliminary experiments were first conducted in 0.1 M HNO_3 to optimize the adsorbent-to-solution ratio, adsorption capacity, and kinetic parameters. An optimal solid-liquid ratio of 0.25 g/L was identified and used in subsequent studies (Figure S13). To quantify the adsorption capacity, isotherm experiments were conducted in 0.1 M HNO_3 at initial Pd(II) concentrations ranging from approximately ~10 to ~1200 ppm (Figure 4a). After 24 h, COF-3 achieved an exceptionally high adsorption capacity of 942.02 ± 24.61 mg/g, which is much higher than those of COF-1 (509.73 ± 9.10 mg/g) and COF-2 (634.98 ± 16.86 mg/g) under identical conditions (Figure 4a). The adsorption isotherms were well fitted by the Langmuir model, indicating a monolayer adsorption process (Figure 4a, Table S4) [42, 43]. As summarized in Figure 4b and Table S5, the adsorption capacity of COF-3 surpasses that of all reported COF adsorbents and most of other adsorbents reported thus far [22, 24, 21, 25–27, 30, 35, 44–62], including commercial sorbents under similar conditions (Figure S14). Adsorption kinetics were further investigated in a 50 ppm Pd(II) (0.1 M HNO_3) solution. COF-3 exhibited rapid adsorption, reaching an adsorption capacity of 168.97 ± 0.03 mg/g within 80 min (Figure 4c). The kinetic data could be fitted well using the pseudo-second-order model, with a high correlation coefficient (R^2), suggesting that chemisorption governs the Pd(II) adsorption process (Figure 4c, Table S6). COF-1 and COF-2 exhibited slower adsorption kinetics under similar conditions. Encouraged by the above mentioned Pd(II) adsorption performance of COF-3, we next conducted experiments in 1 M HNO_3 solutions. COF-3 maintained fast adsorption kinetics and achieved an equilibrium uptake capacity of 642.4 ± 24.32 mg/g in 1 M HNO_3 solutions (Figures S15). Since Pd(II) speciation in nitric acid media can involve hydrated and nitrato-coordinated complexes [63], parallel kinetic and isotherm experiments were further conducted in both 0.1 M and 1 M HNO_3 using $Pd(NO_3)_2{\cdot}2H_2O$ as the Pd source to evaluate the influence of initial Pd speciation. The adsorption capacities and kinetics were very similar to those obtained from Na_2PdCl_4 aqueous solutions. As expected, both adsorption capacities and kinetics followed the order COF-3 > COF-2 > COF-1, indicating that Pd uptake is determined mainly by the intrinsic framework properties rather than the initial Pd(II) source (Figure 4d,e, and Tables S7, S8). Under similar acidic conditions, COF-3 exhibited markedly higher Pd(II) adsorption capacity and faster adsorption kinetics than both hydroxyl-free reference frameworks (Figures 4d,e, S16–S18). These results confirm that hydroxyl groups play a key role in enhancing Pd(II) adsorption under acidic conditions.

The selectivity of COF-3 toward Pd(II) was next evaluated in the presence of competing metal ions using a simulated acidic waste solution (1 M HNO_3) (Table S9). The composition of the competing ions was designed to approximate realistic waste-stream conditions relevant to nuclear fuel reprocessing and metallurgical systems, covering a broad range of ionic species with different charges, coordination behaviors, and concentrations [22, 27, 35, 64]. Specifically, a total of 19 coexisting ions were included, encompassing alkali metal ions (Na^+, Rb^+, Cs^+), alkaline earth metals (Ba^{2+}, Sr^{2+}), transition and post-transition metal ions (Ag^+, Cd^{2+}, Ni^{2+}, Fe^{3+}, Pb^{2+}, Ga^{3+}), lanthanides (La^{3+}, Nd^{3+}, Pr^{3+}, Sm^{3+}, Eu^{3+}, Yb^{3+}), as well as representative anionic species (ReO_4^-), thereby providing a stringent and realistic evaluation environment. Under these conditions, COF-3 exhibited a high removal efficiency exceeding 90%, which is substantially higher than that of all competing metal ions (Figures 4f, S19), demonstrating its strong and highly selective binding affinity toward Pd(II). In contrast, COF-1, COF-2, COF-4, and COF-5 showed significantly lower selectivity under identical conditions, further highlighting the advantage of the charge-density-regulated framework design strategy. In addition, given the importance of Pd/Pt separation in platinum-group metal recovery, binary adsorption experiments were conducted to evaluate the selectivity of COF-3 toward Pd(II) over Pt(IV). The results show that COF-3 exhibits outstanding Pd/Pt separation performance, with a distribution coefficient (K_d) of ~200.27×10^3 mL/g for Pd(II), compared with only ~0.25×10^3 mL/g for Pt(IV), demonstrating its exceptionally high selectivity for Pd over Pt (Figures 4g, S20). Dynamic adsorption performance was subsequently conducted using a packed-column setup with a simulated acidic HLLW solution (~1 M HNO_3; detailed composition is listed in Table S10) [22, 27]. As expected, COF-3 efficiently captured Pd(II), achieving a breakthrough after treating 180 mL of solution and delivering a dynamic adsorption capacity of 261.8 mg/g (Figure 4h). Other metal ions were rapidly eluted from the column, further demonstrating the preferential uptake of Pd(II). To probe the acid tolerance limit of COF-3, adsorption experiments were conducted in 2 M and 3 M HNO_3 solutions. As expected, COF-3 retained appreciable Pd(II) uptake capacities of 550.2 and 476.8 mg/g in 2 M and 3 M HNO_3, respectively (Figure S21), highlighting its robust adsorption capability under harsh acidic environments.

Subsequently, the practical applicability of COF-3 was further evaluated using laboratory-generated palladium-containing waste liquids from chemical synthesis and catalytic studies, which typically contain mixed solvents (e.g., H_2O, EtOH, ACN) and coexisting inorganic ions (e.g., Na^+, UO_2^{2+}, Cl^-, and NO_3^-). Such waste streams represent an important secondary palladium resource, but are challenging to process due to their complex composition. Breakthrough experiment results demonstrated that COF-3 could efficiently capture Pd(II) from these realistic waste liquids, achieving a breakthrough volume of 230 mL and a corresponding dynamic adsorption capacity of 340.6 mg/g (Figure S22). COF-3 further exhibited fast Pd(II) removal ability

15213773, 2026, 33, Downloaded from https://onlinelibrary.wiley.com/doi/10.1002/anie.202402007 by Shengqian Ma - University Of North Texas Willis Library , Wiley Online Library on [21/10/2026]. See the Terms and Conditions (https://onlinelibrary.wiley.com/terms-and-conditions) on Wiley Online Library for rules of use; OA articles are governed by the applicable Creative Commons License

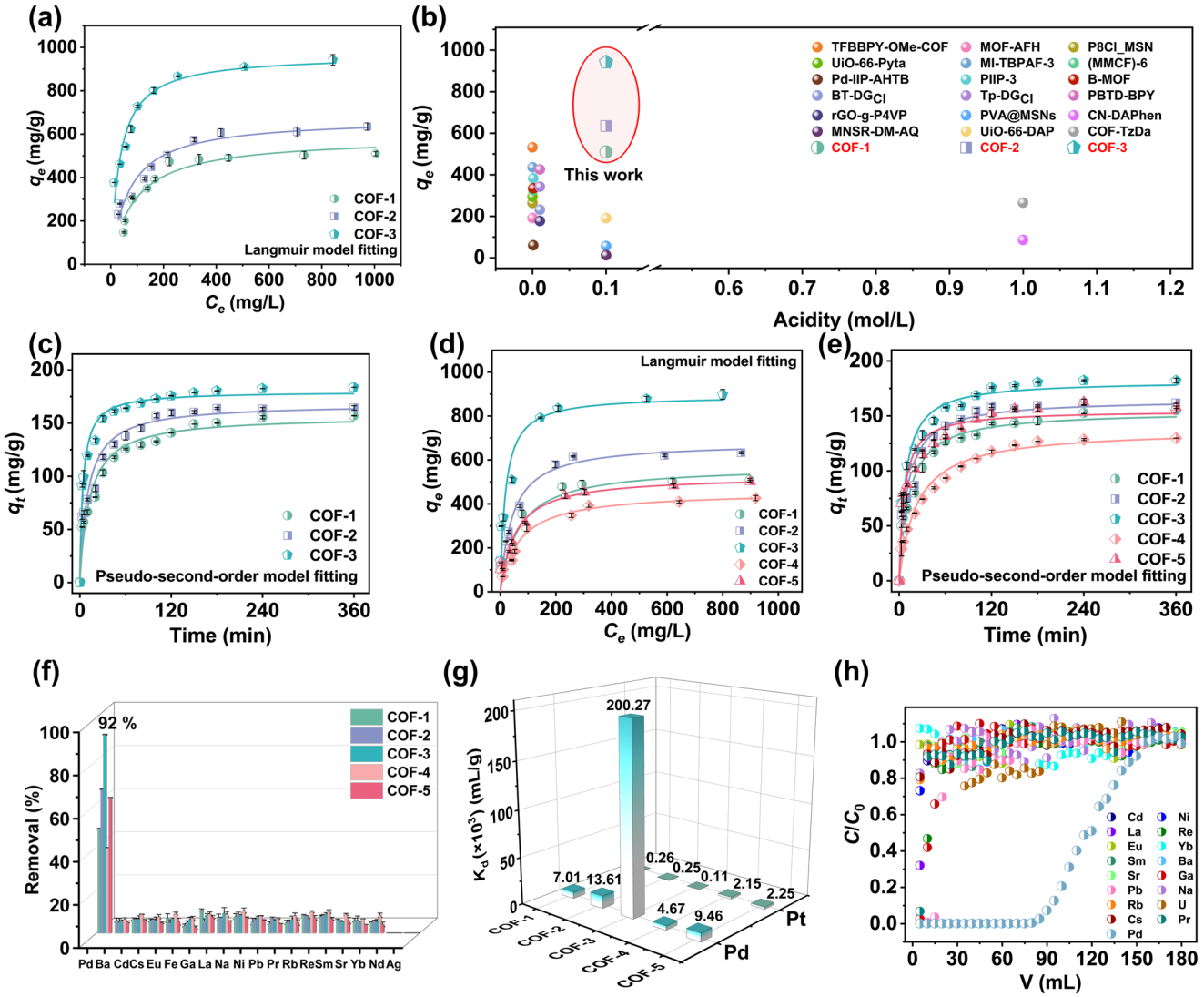


FIGURE 4 | (a) Equilibrium adsorption isotherms for Pd(II) on COF-1, COF-2, and COF-3 in 0.1 M HNO_3 solutions at initial Pd(II) concentrations of 80–1000 ppm. (b) Comparison of reported saturated Pd(II) uptake capacities for various adsorbents. The data were collected from studies performed under different experimental conditions, and detailed parameters are summarized in Table S5 in the Supporting Information. (c) Pd(II) adsorption kinetics on COF-1, COF-2, and COF-3 at an initial Pd(II) concentration of ~50 ppm. (d) Equilibrium adsorption isotherms for Pd(II) on COF-1, COF-2, COF-3, COF-4, and COF-5 in 0.1 M HNO_3 solutions using $Pd(NO_3)_2{\cdot}2H_2O$ as the Pd source, fitted with the Langmuir model. (e) Adsorption kinetics of Pd(II) on COF-1, COF-2, COF-3, COF-4, and COF-5 in 0.1 M HNO_3 at an initial Pd(II) concentration of ~50 ppm, using $Pd(NO_3)_2{\cdot}2H_2O$ as the Pd source. (f) Removal efficiencies of COF-1, COF-2, COF-3, COF-4, and COF-5 toward different competing metal ions in a multicomponent solution (acidity ~1 M HNO_3). (g) Distribution coefficient (K_d) for Pd(II) and Pt(IV) in a Pd/Pt separation using COF-1, COF-2, COF-3, COF-4, and COF-5. (h) Experimental column breakthrough curves for simulated HLLW solution (acidity ~1 M HNO_3) by COF-3.

from low concentration Pd solutions (from ~5 ppm to ~10 ppb in aqueous HNO_3), indicating COF-3 would be a very promising adsorbent for palladium recovery (Figure S23). We carried out further adsorption experiments using low and trace-level aqueous palladium solutions (~1000, 500, 100, and 50 ppb Pd(II)). Commercial adsorbents including Al_2O_3, IRA-4200, IRA-402, D101, and D311 were used for comparison. As expected, COF-3 demonstrated rapid Pd(II) uptake at low concentrations, reaching over 99% of its equilibrium adsorption capacity in ~1000, 500, 100, and 50 ppb Pd(II) solutions, respectively (Figure S24). Commercial Al_2O_3, IRA-4200, IRA-402, D101, and D311 showed lower Pd(II) uptakes under similar conditions (in a ~500 ppb Pd(II) solution). These results further highlight the practical potential of COF-3 for Pd(II) recovery from realistic wastewater streams containing trace amounts of palladium. Notably, the adsorbed Pd(II) could be readily eluted from COF-3 using a mixed solution of 0.5 M thiourea and 0.5 M HCl. The Pd(II) removal efficiency remained at ~90% after five consecutive adsorption-desorption cycles and still reached ~75% after 10 cycles (Figure S25). The gradual decrease in removal efficiency may be attributed to incomplete desorption of Pd(II), sample loss, and partial loss of accessible binding sites during repeated adsorption-elution cycles. PXRD, FT-IR, and BET analyses were further carried out after the fifth and 10th cycles to assess structural stability. Even after repeated regeneration, COF-3 retained high crystallinity and largely preserved its surface area and pore structure, demonstrating good framework robustness during cycling (Figure S26). These results demonstrate that COF-3 integrates high adsorption

15213773, 2026, 33, Downloaded from https://onlinelibrary.wiley.com/doi/10.1002/anie.202402007 by Shengqian Ma - University Of North Texas Willis Library , Wiley Online Library on [21/10/2026]. See the Terms and Conditions (https://onlinelibrary.wiley.com/terms-and-conditions) on Wiley Online Library for rules of use; OA articles are governed by the applicable Creative Commons License

capacity, rapid kinetics, excellent selectivity, and robust reusability under strongly acidic conditions, underscoring its potential as an efficient adsorbent for palladium recovery from high-level radioactive waste liquids and realistic laboratory waste streams.

2.3 | Adsorption Mechanism

To gain a deeper understanding of the distinct Pd(II) adsorption behaviors observed for COF-1, COF-2, and COF-3 under acidic conditions, X-ray photoelectron spectroscopy (XPS), synchrotron-based extended X-ray absorption near edge spectroscopy (XANES), extended X-ray absorption fine structure (EXAFS), and DFT calculations were systematically employed to probe the chemical state, coordination environment, and electronic structure of adsorbed Pd(II) within the frameworks. The Pd 3d XPS spectra of COF-1, COF-2, and COF-3 after Pd(II) uptake exhibited characteristic Pd $3d_{5/2}$ and Pd $3d_{3/2}$ peaks at approximately 338.2 and 343.4 eV, respectively, with no detectable Pd(0) signal (Figures S27–S31), indicating that Pd(II) remained in the divalent oxidation state upon adsorption. Distinct differences in oxygen and nitrogen chemical environments were observed among the three COFs after Pd(II) adsorption. The O 1s spectrum of COF-1 displayed an obvious ketone oxygen (—C═O) signal at 532.2 eV [65], together with the emergence of a new N 1s peak (—N—H) near 400.2 eV (Figures 5a, S27), indicating enol-keto tautomerization of the hydroxyl groups and concurrent protonation of the imine N atoms under acidic conditions, consistent with previous reports [27, 65]. No —C═O signal was detected in the O 1s spectra of COF-2 and COF-3 after Pd(II) adsorption (Figures S28, S30), demonstrating that enol-keto tautomerism did not occur in these frameworks. More importantly, a distinct N 1s signal corresponding to protonated imine nitrogen (C═N^+—H, ~402.5 eV) was observed only for COF-1 after Pd(II) adsorption, whereas this feature was absent in both COF-2 and COF-3 (Figure 5a). This result indicates that imine nitrogen atoms in COF-2 and COF-3 tend to remain unprotonated under acidic conditions, demonstrating that increased local charge density effectively suppresses protonation of imine N sites. Furthermore, a N 1s signal at ~406.8 eV was observed in COF-1, attributed to nitrate coordination (Figure 5a). No chloride signals were detected in COF-1 (Figure S27). Instead, Cl^- signals with Cl $2p_{3/2}$ binding energies ~198.2 and ~198.4 eV was detected in COF-2 and COF-3, respectively, without the presence of nitrate signals (Figures S28–S30). Results suggested that nitrate anions participate in Pd(II) coordination in COF-1, whereas chloride ions are involved in Pd(II) coordination in COF-2 and COF-3. To further verify the suppression of acid-induced imine protonation, COF-1, COF-2, and COF-3 were treated with HNO_3 in the absence of Pd(II). After being treated in a 0.1 M HNO_3 solution, XPS analysis revealed a pronounced C═N^+—H signal at ~402.7 eV for COF-1, a much weaker signal for COF-2, and no obvious signal for COF-3 (Figure S32), indicating progressively reduced protonation [27, 66]. Protonation-related signals were also observed for the hydroxyl-free reference frameworks COF-4 and COF-5. FT-IR spectra further showed that the imine C═N band of COF-1 at 1613 cm^{-1} shifted to ~1643 cm^{-1} after treatment in 0.1 M HNO_3, corresponding to protonated C═N^+—H species, and disappeared after 3 M HNO_3 treatment, suggesting extensive protonation (Figure S33) [66–68]. COF-2 showed a weaker acid-induced shift, whereas the C═N band of COF-3 at ~1620 cm^{-1} was retained even after treatment in 3 M HNO_3 [66–68]. The hydroxyl-free reference COFs showed consistent protonation behavior. COF-4 was readily protonated, with its C═N band disappearing after treatment with 0.1 M HNO_3 and a new C═N^+—H band appearing at ~1654 cm^{-1}. COF-5 also showed acid-induced protonation, with its C═N band shifting from ~1616 to ~1639 cm^{-1} and disappearing after 3 M HNO_3 treatment (Figure S33). Raman spectra further supported this trend by revealing a new band at ~1665 cm^{-1}, assignable to C═N^+—H stretching, in COF-1, COF-2, COF-4, and COF-5 after treatment with 0.1 M HNO_3 [68]. No such signals were observed in COF-3 after HNO_3 treatment (Figures 5b,c, S34). Taken together, these results provide direct spectroscopic evidence that imine protonation is strongly suppressed in COF-3, supporting the proposed charge-density-regulated protonation mechanism.

We next conducted the Pd K-edge X-ray absorption fine structure (XAFS) analysis to further understand the coordination environment of Pd(II) in COF-3. The XANES spectrum of Pd-loaded COF-3 closely resembles those of the PdO and $PdCl_2$ reference compounds, rather than that of metallic Pd foil, further confirming the existence of the Pd(II) oxidation state after adsorption (Figure 5d). The Fourier-transformed EXAFS spectra of COF-3 exhibit a dominant contribution in the first coordination shell, with features appearing at approximately 1.5–2.0 Å in R space (uncorrected for phase shift), consistent with Pd-ligand interactions (Figure 5e,f). Quantitative EXAFS fitting resolves this first-shell contribution into Pd-N/O and Pd-Cl scattering paths, yielding average bond lengths of ~2.0 Å for Pd-N/O and ~2.3 Å for Pd-Cl, respectively (Figure 5g, Table S11). The coordination number extracted from the fitting analysis indicates that Pd(II) is coordinated by approximately four neighboring atoms, consistent with a square-planar coordination environment involving framework N/O donors and chloride ligands. Collectively, XPS and EXAFS analyses suggest that control of imine nitrogen protonation is the primary factor tuning Pd(II) binding affinity under acidic conditions, whereas enol-keto tautomerization contributes only a limited number of oxygen-based coordination sites within specific structural environments. This distinction stems from the fact that enol-keto tautomerism generates only a limited number of oxygen-based coordination sites and only within specific structural environments, whereas imine N atoms represent the intrinsic and most abundant binding sites in imine-linked COFs. Once protonated under acidic conditions, these nitrogen sites lose their electron-donating capacity, making them unavailable for coordinating metal ions and substantially reducing the total number of metal binding sites. In contrast, suppression of imine N protonation preserves the framework's inherent coordination functionality and allows these sites to participate directly in Pd(II) binding. The progressive decrease in protonated-N species from COF-1 to COF-3, therefore, correlates directly with enhanced Pd(II) adsorption performance, highlighting imine N protonation as the dominant factor controlling site availability and adsorption efficiency under acidic conditions. Next, DFT calculations were performed to theoretically investigate the electronic properties of the three COFs and their Pd(II) binding behaviors. Compared with COF-1 and COF-2, electrostatic potential (ESP) mapping shows that COF-3 presents a more concentrated negative potential on its van der Waals surface, indicating stronger local electron enrichment around the binding region (Figure 5h). Notably, the minimum ESP value near the ortho-hydroxyl site in

15213773, 2026, 33, Downloaded from https://onlinelibrary.wiley.com/doi/10.1002/anie.202412007 by Shengqian Ma - University Of North Texas Willis Library , Wiley Online Library on [21/10/2026]. See the Terms and Conditions (https://onlinelibrary.wiley.com/terms-and-conditions) on Wiley Online Library for rules of use; OA articles are governed by the applicable Creative Commons License

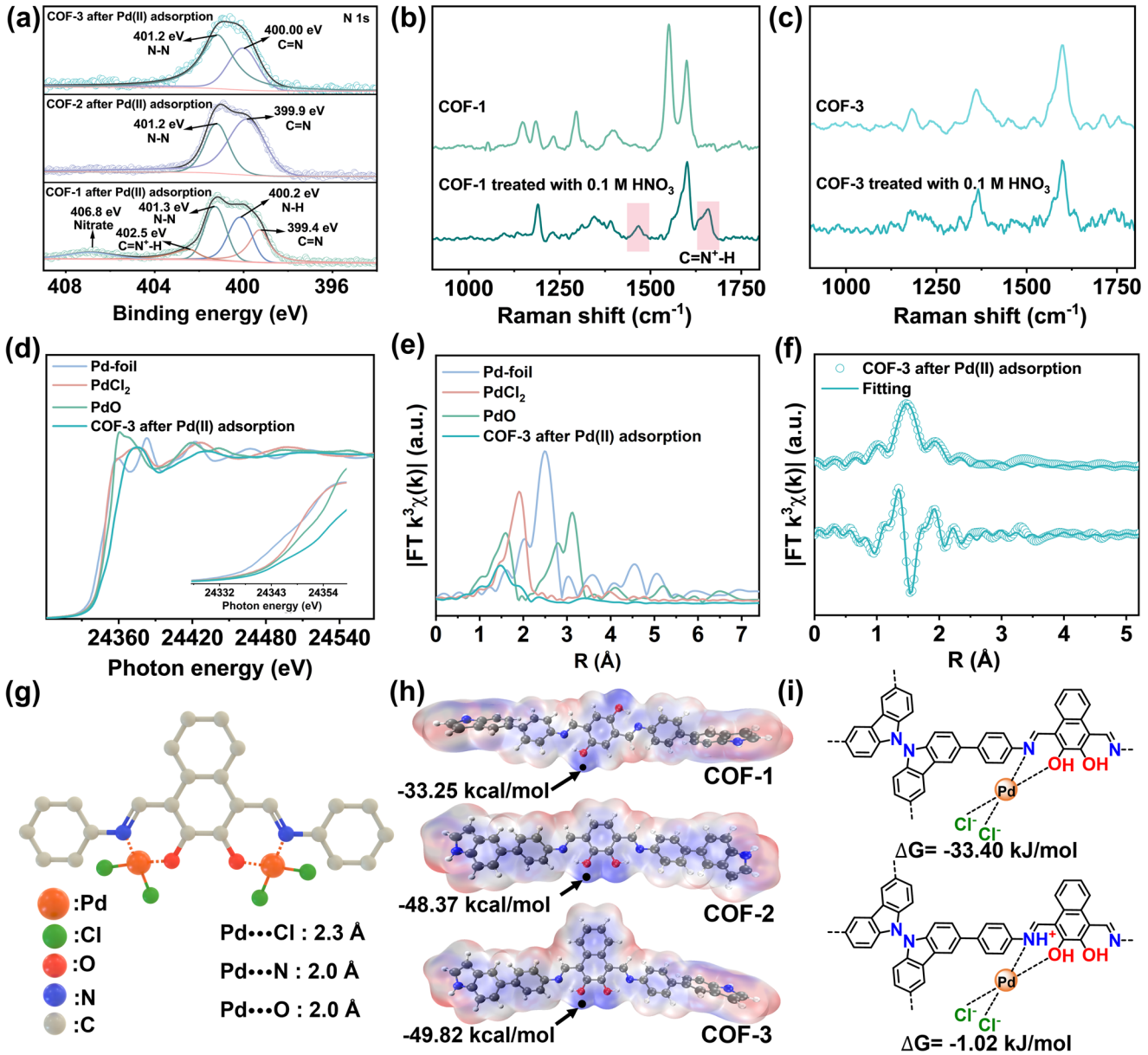


FIGURE 5 | (a) N 1s XPS spectra of COF-1, COF-2, and COF-3 after adsorption of Pd(II). (b) Raman spectra of COF-1 before and after treatment with 0.1 M HNO_3. (c) Raman spectra of COF-3 before and after treatment with 0.1 M HNO_3. (d) Pd K-edge XANES spectra for COF-3 after adsorption of Pd(II) and selected reference samples. (e) Pd K-edge EXAFS spectra for COF-3 after adsorption of Pd(II) and selected reference samples. (f) EXAFs fitting curves for COF-3 after adsorption of Pd(II). (g) COF-3 structure used as a model for the EXAFS analysis. The Pd atom (dark green sphere) is bound with one N atom (blue spheres), one O atom (pink sphere) from COF-3, and two chlorine atoms to form a square-planar [Pd(II)$NOCl_2$] unit. (h) Electrostatic potential (ESP) of COF-1, COF-2, and COF-3. (i) Models for Pd(II) binding to different sites in COF-3 and the corresponding Gibbs free energy changes (ΔG).

COF-3 (−49.82 kcal/mol) is more negative than those of COF-1 (−33.25 kcal/mol) and COF-2 (−48.37 kcal/mol), consistent with the enhanced local charge density. For comparison, the reference framework COF-5 exhibits a much less negative ESP minimum (-29.18 kcal/mol), further supporting the correlation between increased local charge density and the experimentally observed enhanced protonation resistance (Figure S35). This calculated trend agrees well with the XPS, FT-IR, and Raman results, which show progressively suppressed imine protonation from COF-1 to COF-3, confirming that enhanced local charge density helps preserve accessible Pd(II)-binding sites under acidic conditions (Figures 5a–c, S32–34). To further probe the binding preference, representative Pd(II) coordination modes in COF-3 were modeled, and their Gibbs free energy changes (ΔG) were calculated (Figure 5i). Among the geometries considered, the configuration in which Pd(II) is coordinated by one hydroxyl oxygen and one imine nitrogen from the framework, together with two chloride ligands, yields the lowest ΔG, suggesting a thermodynamically favored square-planar [Pd(II)$NOCl_2$] coordination environment, consistent with the spectroscopic results. Overall, these calculations support the conclusion that regulating local charge density can mitigate imine nitrogen protonation under acidic conditions, thereby improving binding site availability and boosting selective Pd(II) capture.

15213773, 2026, 33, Downloaded from https://onlinelibrary.wiley.com/doi/10.1002/anie.202402007 by Shengqian Ma - University Of North Texas Willis Library , Wiley Online Library on [21/10/2026]. See the Terms and Conditions (https://onlinelibrary.wiley.com/terms-and-conditions) on Wiley Online Library for rules of use; OA articles are governed by the applicable Creative Commons License

Taken together, this study identifies acid-induced protonation of the imine N as a fundamental bottleneck limiting the performance of imine-linked COFs for Pd(II) recovery in realistic acidic environments. To address this challenge, we strategically positioned hydroxyl groups on the same side of the aromatic rings and incorporated naphthalene units into the COF structure, thereby tuning the local charge density at the imine N sites, suppressing nitrogen protonation under acidic conditions. Unlike strategies that rely on generating auxiliary functional groups, this approach directly targets site deactivation at its electronic origin and allows full utilization of the inherent framework functionalities. As a representative example, one of our synthesized COFs (COF-3) exhibits outstanding Pd(II) adsorption performance under various acidic conditions. Spectroscopic and computational analyses reveal that Pd(II) binding proceeds through cooperative N—O coordination, forming stable square-planar complexes that involve both imine nitrogen and adjacent oxygen donors, rather than relying solely on oxygen-based or interlayer-derived sites. This synergistic coordination mode significantly increases the population of effective binding sites, explaining the high capacity, rapid adsorption kinetics, and excellent selectivity observed in Pd(II) adsorption experiments on COF-3. Overall, both experimental evidence and theoretical analysis demonstrate that suppressing protonation-induced site deactivation in imine-linked COFs by tuning the local charge density is an effective strategy for achieving high Pd(II) adsorption capacities in acidic media. This strategy offers a new paradigm for the rational design of high-performance adsorbents aimed at the selective recovery of precious metals from acidic and complex waste streams.

3 | Conclusion

In summary, we have designed and successfully synthesized a family of imine-linked COF adsorbents by systematically tuning the local charge density at a molecular level. The experimental and theoretical studies verified that increasing the electron cloud density around imine N atoms can significantly reduce protonation at such sites in acidic media, thereby preserving a high density of accessible binding sites for Pd(II). One of our developed COFs, COF-3, possessed an extremely high Pd(II) adsorption capacity, state-of-the-art performance for any COF adsorbents in acidic solutions. Our work lays a platform for the design of improved COF adsorbents for precious metal recovery from acidic waste streams.

Author Contributions

Shijie Xiong: methodology, data curation, investigation, and writing – review and editing. **Pei Chen**: methodology, data curation, investigation, and writing – review and editing. **Hanzhi Chen**: methodology, data curation, writing – original draft, and writing – review and editing. **Muliang Xiao**: visualization, writing – review and editing. **Ruining Cao**: writing – review and editing. **Jiaqi Li**: writing – review and editing. **Chuanlei Luo**: writing – review and editing. **Xinyi Yang**: writing – review and editing. **Xiaolu Liu**: writing – review and editing, visualization. **Yinghui Xie**: writing – review and editing, visualization. **Mengjie Hao**: writing – review and editing. **Geoffrey I. N. Waterhouse**: writing – review and editing. **Xiangke Wang**: writing – review and editing, conceptualization, supervision, and funding acquisition. **Shengqian Ma**: writing – review and editing, and conceptualization. **Hui Yang**: conceptualization, validation, writing – review and editing, writing – original draft, supervision, and funding acquisition.

Acknowledgments

The authors gratefully acknowledge funding support from the National Natural Science Foundation of China (Grants U24B20195; 22322603; 22506048), the Beijing Outstanding Young Scientist Program (Hui Yang, Mengjie Hao, and Xiangke Wang). The Robert A. Welch Foundation (B-0027) Shengqian Ma is also acknowledged. Geoffrey I. N. Waterhouse acknowledges funding support from the MacDiarmid Institute for Advanced Materials and Nanotechnology. We also thank the Guangzhou Huaxi Testing Technology Center for expert assistance with X-ray absorption spectroscopy measurements and for providing reference data of Pd-foil, $PdCl_2$, and PdO standards.

Conflicts of Interest

The authors declare no competing interest.

Data Availability Statement

The data that support the findings of this study are available on request from the corresponding author. The data are not publicly available due to privacy or ethical restrictions

References

1. S. McCarthy, D. C. Braddock, and J. D. E. T. Wilton-Ely, "Strategies for Sustainable Palladium Catalysis," *Coordination Chemistry Reviews* 442 (2021): 213925, https://doi.org/10.1016/j.ccr.2021.213925.

2. D. Jiang, G. Wan, J. Halldin Stenlid, et al., "Dynamic and Reversible Transformations of Subnanometre-Sized Palladium on Ceria for Efficient Methane Removal," *Nature Catalysis* 6 (2023): 618–627, https://doi.org/10.1038/s41929-023-00983-8.

3. J. Wang and G. Dong, "Palladium/Norbornene Cooperative Catalysis," *Chemical Reviews* 119 (2019): 7478–7528, https://doi.org/10.1021/acs.chemrev.9b00079.

4. H. Wu, Q. Pan, J. Grill, M. J. Johansson, Y. Qiu, and J.-E. Bäckvall, "Palladium-Catalyzed Oxidative Allene–Allene Cross-Coupling," *Journal of the American Chemical Society* 147 (2025): 4338–4348, https://doi.org/10.1021/jacs.4c14607.

5. Y. Li, L. Loh, S. Li, et al., "Anomalous Resistive Switching in Memristors Based on Two-Dimensional Palladium Diselenide Using Heterophase Grain Boundaries," *Nature Electronics* 4 (2021): 348–356, https://doi.org/10.1038/s41928-021-00573-1.

6. Y. Wang, J. Niu, L. Bu, E.-Q. Li, and T.-P. Loh, "Recent Advances in Palladium-Catalyzed Cyclizations for the Synthesis of Spirooxindoles," *Coordination Chemistry Reviews* 547 (2026): 217145, https://doi.org/10.1016/j.ccr.2025.217145.

7. M. R. Uehling, R. P. King, S. W. Krska, T. Cernak, and S. L. Buchwald, "Pharmaceutical Diversification via Palladium Oxidative Addition Complexes," *Science* 363 (2019): 405–408, https://doi.org/10.1126/science.aac6153.

8. L. Li, Z. Cai, Q. Wu, et al., "Rational Design of Porous Conjugated Polymers and Roles of Residual Palladium for Photocatalytic Hydrogen Production," *Journal of the American Chemical Society* 138 (2016): 7681–7686, https://doi.org/10.1021/jacs.6b03472.

9. B. M. Tackett, J. H. Lee, and J. G. Chen, "Electrochemical Conversion of CO_2 to Syngas With Palladium-Based Electrocatalysts," *Accounts of Chemical Research* 53 (2020): 1535–1544, https://doi.org/10.1021/acs.accounts.0c00277.

10. D. I. Kim, G. Gwak, P. Dorji, et al., "Palladium Recovery Through Membrane Capacitive Deionization From Metal Plating Wastewater," *ACS Sustainable Chemistry & Engineering* 6 (2018): 1692–1701, https://doi.org/10.1021/acssuschemeng.7b02923.

15213773, 2026, 33, Downloaded from https://onlinelibrary.wiley.com/doi/10.1002/anie.202412007 by Shengqian Ma - University Of North Texas Willis Library , Wiley Online Library on [21/10/2026]. See the Terms and Conditions (https://onlinelibrary.wiley.com/terms-and-conditions) on Wiley Online Library for rules of use; OA articles are governed by the applicable Creative Commons License

11. J. Xiong, Y. Zhang, Y. Chen, et al., "Cost-effective and High-Performance Biguanide-Incorporated Ionic Porous Organic Polymer for Selective Recovery of Pd(II) and Pt(IV) From Metallurgical Wastewater," *Chemical Engineering Journal* 488 (2024): 150772, https://doi.org/10.1016/j.cej.2024.150772.

12. N. Cheng, L. Zhang, M. Wang, et al., "Highly Effective Recovery of Palladium From a Spent Catalyst by an Acid- and Oxidation-resistant Electrospun Fibers as a Sorbent," *Chemical Engineering Journal* 466 (2023): 143171, https://doi.org/10.1016/j.cej.2023.143171.

13. L. Zhang, Q. Song, Y. Liu, and Z. Xu, "Novel Approach for Recovery of Palladium in Spent Catalyst From Automobile by a Capture Technology of Eutectic Copper," *Journal of Cleaner Production* 239 (2019): 118093, https://doi.org/10.1016/j.jclepro.2019.118093.

14. Z. Chang, Y. Zhou, P. Shao, et al., "Proton-Driven Multistage System Enables Selective Recovery of Gold and Palladium From Electronic Waste Leachate," *Energy & Environmental Materials* 9 (2026): e70085, https://doi.org/10.1002/eem2.70085.

15. M. Bigum, L. Brogaard, and T. H. Christensen, "Metal Recovery From High-Grade WEEE: A Life Cycle Assessment," *Journal of Hazardous Materials* 207-208 (2012): 8–14, https://doi.org/10.1016/j.jhazmat.2011.10.001.

16. H. Wu, S.-Y. Kim, M. Miwa, and S. Matsuyama, "Synergistic Adsorption Behavior of a Silica-Based Adsorbent Toward Palladium, Molybdenum, and Zirconium From Simulated High-Level Liquid Waste," *Journal of Hazardous Materials* 411 (2021): 125136, https://doi.org/10.1016/j.jhazmat.2021.125136.

17. R. Ruhela, A. K. Singh, B. S. Tomar, and R. C. Hubli, "Separation of Palladium From High Level Liquid Waste—A Review," *RSC Advances* 4 (2014): 24344, https://doi.org/10.1039/c4ra02024c.

18. Z. Mohammadi Zardkhoshouei, A. Moghaddam, M. Naqvi, et al., "Recent Advances in Precious Metal Recovery Using Porous Organic Materials: From Structure to Mechanisms," *Coordination Chemistry Reviews* 548 (2026): 217202, https://doi.org/10.1016/j.ccr.2025.217202.

19. K. Leopold, A. Denzel, A. Gruber, and L. Malle, "Mobility of Traffic-Related Pd and Pt Species in Soils Evaluated by Sequential Extraction," *Environmental Pollution* 242 (2018): 1119–1127, https://doi.org/10.1016/j.envpol.2018.07.130.

20. J. Fang, Y. Jiang, X.-P. Yan, and Z.-M. Ni, "Selective Quantification of Trace Palladium in Road Dusts and Roadside Soils by Displacement Solid-Phase Extraction Online Coupled With Electrothermal Atomic Absorption Spectrometry," *Environmental Science & Technology* 39 (2005): 288–292, https://doi.org/10.1021/es049303+.

21. Y. Song, G. Verma, K. Tan, et al., "Tailoring the Coordination Micro-Environment in Nanotraps for Efficient Platinum/Palladium Separation," *Advanced Materials* 36 (2024): 2313747, https://doi.org/10.1002/adma.202313747.

22. Y. Xie, Q. Rong, C. Wen, et al., "Covalent Organic Framework With Predesigned Single-Ion Traps for Highly Efficient Palladium Recovery From Wastes," *CCS Chemistry* 6 (2024): 1908–1919, https://doi.org/10.31635/ccschem.023.202303404.

23. A. Zhang, W. Xue, and X. Dong, "Development of Palladium Separation Process From Nitric Acid Medium Utilizing a New Hybrid Multi-Nitrogen Adsorbent," *Separation and Purification Technology* 189 (2017): 220–228, https://doi.org/10.1016/j.seppur.2017.07.057.

24. B. Aguila, Q. Sun, H. C. Cassady, et al., "A Porous Organic Polymer Nanotrap for Efficient Extraction of Palladium," *Angewandte Chemie International Edition* 59 (2020): 19618–19622, https://doi.org/10.1002/anie.202006596.

25. J. Ren, Y. Ye, Y. Zhang, et al., "Metal-Macrocyclic Framework Featuring Adaptive Cavity for Precise Palladium Recognition," *Chemistry* 10 (2024): 2776–2791, https://doi.org/10.1016/j.chempr.2024.04.016.

26. J. Tang, Y. Chen, S. Wang, D. Kong, and L. Zhang, "Highly Efficient Metal-Organic Frameworks Adsorbent for Pd(II) and Au(III) Recovery From Solutions: Experiment and Mechanism," *Environmental Research* 210 (2022): 112870, https://doi.org/10.1016/j.envres.2022.112870.

27. Y. Bai, L. Chen, L. He, et al., "Precise Recognition of Palladium Through Interlaminar Chelation in a Covalent Organic Framework," *Chemistry* 8 (2022): 1442–1459, https://doi.org/10.1016/j.chempr.2022.02.016.

28. H. Liu, P. Wu, K. Wang, et al., "Palladium Recovery From Acidic Solution With Phenanthroline-Based Covalent Organic Polymers as Adsorbents for Efficient Heterogeneous Catalysis," *Green Chemistry* 26 (2024): 804–814, https://doi.org/10.1039/D3GC03851C.

29. A. Volkov, J. Mi, K. Lalit, et al., "General Strategy for Incorporation of Functional Group Handles Into Covalent Organic Frameworks via the Ugi Reaction," *Journal of the American Chemical Society* 145 (2023): 6230–6239, https://doi.org/10.1021/jacs.2c12440.

30. A. Meng, H. Yan, J. Zhu, et al., "Covalent Organic Polymers Based on Triazine-Pyridyl Group for High Capacity and High Selectivity Removal of Pd(II)," *Separation and Purification Technology* 360 (2025): 130870, https://doi.org/10.1016/j.seppur.2024.130870.

31. I. Ahmed and S. H. Jhung, "Covalent Organic Framework-Based Materials: Synthesis, Modification, and Application in Environmental Remediation," *Coordination Chemistry Reviews* 441 (2021): 213989, https://doi.org/10.1016/j.ccr.2021.213989.

32. R. Liu, K. T. Tan, Y. Gong, et al., "Covalent Organic Frameworks: An Ideal Platform for Designing Ordered Materials and Advanced Applications," *Chemical Society Reviews* 50 (2021): 120–242, https://doi.org/10.1039/D0CS00620C.

33. M. Bashri, S. Kumar, P. Bhandari, et al., "Hydrazone-Linked Covalent Organic Framework Catalyst via Efficient Pd Recovery From Wastewater," *ACS Applied Materials & Interfaces* 17 (2024): 17804–17812, https://doi.org/10.1021/acsami.4c07706.

34. S. Cao, D. Li, A. A. Uliana, et al., "Multifunctional Covalent Organic Framework Membranes With an Ultrathin Recycled Palladium Nanolayer for Efficient Water Decontamination," *Applied Catalysis B: Environmental* 323 (2023): 122175, https://doi.org/10.1016/j.apcatb.2022.122175.

35. Y. Cai, Q. Li, D. Xu, et al., "Bioinspired Skeleton-and-Pore Regulation of Covalent Organic Frameworks for High-Capacity and Ultrarapid Palladium Recovery," *Advanced Functional Materials* 36 (2025): e23648, https://doi.org/10.1002/adfm.202523648.

36. Z. Li, Z. Dong, Z. Zhang, et al., "Covalent Organic Frameworks for Boosting H_2 O_2 Photosynthesis via the Synergy of Multiple Charge Transfer Channels and Polarized Field," *Angewandte Chemie International Edition* 64 (2024): e202420218, https://doi.org/10.1002/anie.202420218.

37. W. Y. Zhong, M. Wang, H. Hu, et al., "Ultrahigh-efficient N,O-functionalized covalent organic framework towards thorium adsorption from uranium and rare earth elements," *Separation and Purification Technology* 347 (2024): 11, https://doi.org/10.1016/j.seppur.2024.127603.

38. H. J. Shi, Z. J. Zhang, Y. G. Ouyang, et al., "Lewis base anchored DhaTph covalent-organic framework for effective capture of thorium(IV) ion," *Separation and Purification Technology* 328 (2024): 8, https://doi.org/10.1016/j.seppur.2023.125021 .

39. A. F. M. El-Mahdy, M.-Y. Lai, and S.-W. Kuo, "A Highly Fluorescent Covalent Organic Framework as a Hydrogen Chloride Sensor: Roles of Schiff Base Bonding and π-stacking," *Journal of Materials Chemistry C* 8 (2020): 9520–9528, https://doi.org/10.1039/D0TC01872D.

40. C. Chen, L. Cao, Y. Liu, et al., "Investigating a Seemingly Simple Imine-Linked Covalent Organic Framework Structure," *Journal of the American Chemical Society* 146 (2024): 35504–35512, https://doi.org/10.1021/jacs.4c16678.

41. Y. Zhang, Q. Ma, H. Zhang, et al., "Iodine Doping Covalent Organic Frameworks to Reduce Electron-Hole Recombination for Promoting Photocatalytic Performance," *Science Bulletin* 71 (2026): 388–398, https://doi.org/10.1016/j.scib.2025.12.002.

15213773, 2026, 33, Downloaded from https://onlinelibrary.wiley.com/doi/10.1002/anie.202420078 by Shengqian Ma - University Of North Texas Willis Library , Wiley Online Library on [21/10/2026]. See the Terms and Conditions (https://onlinelibrary.wiley.com/terms-and-conditions) on Wiley Online Library for rules of use; OA articles are governed by the applicable Creative Commons License

42. L. Yin, B. Hu, L. Zhuang, et al., "Synthesis of Flexible Cross-linked Cryptomelane-Type Manganese Oxide Nanowire Membranes and Their Application for U(VI) and Eu(III) Elimination From Solutions," *Chemical Engineering Journal* 381 (2020): 122744, https://doi.org/10.1016/j.cej.2019.122744.

43. P. Gu, S. Zhang, C. Zhang, et al., "Two-Dimensional MAX-Derived Titanate Nanostructures for Efficient Removal of Pb(ii)," *Dalton Transactions* 48 (2019): 2100–2107, https://doi.org/10.1039/C8DT04301A.

44. F. Wu, H. Li, Y. Pan, Y. Sun, and J. Pan, "Bioinspired construction of magnetic nano stirring rods with radially aligned dual mesopores and intrinsic rapid adsorption of palladium," *Journal of Hazardous Materials* 441 (2023): 129917, https://doi.org/10.1016/j.jhazmat.2022.129917.

45. Y. Liu, W. Guo, J. Liu, et al., "Bipyridine Covalent Organic Framework Aerogel for Highly Selective Recovery of Palladium in Wastewater," *Chemical Science* 16 (2025): 5745–5754, https://doi.org/10.1039/D4SC08674K.

46. F. Liu, Z. Li, F. Xia, and B. Hu, "Efficient Recovery of Pd(II) From Nuclear Wastewater Using a Functionalized Covalent Organic Frameworks With Uniform Spherical Structure: Size Control, Performance and Mechanism Insight," *Separation and Purification Technology* 359 (2025): 130357, https://doi.org/10.1016/j.seppur.2024.130357.

47. P. Wu, H. Liu, M. Sun, et al., "Covalent Triazine Frameworks for the Selective Sorption of Palladium From Highly Acidic Radioactive Liquid Wastes," *Journal of Materials Chemistry A* 9 (2021): 27320–27331, https://doi.org/10.1039/D1TA04590C.

48. L. Peng, M. Zhang, Z. Dong, W. Qi, M. Zhai, and L. Zhao, "Efficient and Selective Adsorption of Pd(II) by Amino Acid-Functionalized Cellulose Microspheres and Their Applications in Palladium Recovery From PCBs Leaching Solution," *Separation and Purification Technology* 301 (2022): 122037, https://doi.org/10.1016/j.seppur.2022.122037.

49. N. F. Khusnun, N. S. Hasan, I. Amalina, A. A. Jalil, and M. L. Firmansyah, "Enhanced Recovery of Palladium From an Aqueous Solution Using an Ionic Liquid–Mesoporous Silica Composite in Batch and Fixed-Column Studies," *Industrial & Engineering Chemistry Research* 61 (2022): 8634–8644, https://doi.org/10.1021/acs.iecr.2c01258.

50. M. Zha, J. Liu, Y.-L. Wong, and Z. Xu, "Extraction of Palladium From Nuclear Waste-Like Acidic Solutions by a Metal–Organic Framework With Sulfur and Alkene Functions," *Journal of Materials Chemistry A* 3 (2015): 3928–3934, https://doi.org/10.1039/C4TA06678B.

51. L. Zhao, X. Ma, J. Xiong, et al., "Guanidinium-functionalized Ionic Covalent Organic Framework for Selective and Efficient Recovery of Palladium(II) From Metallurgical Wastewater," *Journal of Environmental Chemical Engineering* 11 (2023): 110549, https://doi.org/10.1016/j.jece.2023.110549.

52. J. C. Yin, X. Lian, Z. G. Li, et al., "Triazacoronene-Based 2D Conductive Metal–Organic Framework for High-Capacity Lithium Storage," *Advanced Functional Materials* 34 (2024): 2403656, https://doi.org/10.1002/adfm.202403656.

53. Y. Chen, P. Zhang, Y. Yang, et al., "Porous g-C_3N_4 modified with phenanthroline diamide for efficient and ultrafast adsorption of palladium from simulated high level liquid waste," *Environmental Science: Nano* 10 (2023): 295–310, https://doi.org/10.1039/D2EN00868H .

54. K. S. Song, T. Ashirov, S. N. Talapaneni, et al., "Porous Polyisothiocyanurates for Selective Palladium Recovery and Heterogeneous Catalysis," *Chemistry* 8 (2022): 2043–2059, https://doi.org/10.1016/j.chempr.2022.05.009.

55. J. Feng, M. Xie, D. Xu, et al., "Preparation of Metal-Organic Framework Composite Beads for Selective Adsorption and Separation of Palladium: Properties, Mechanism and Practical Application," *Separation and Purification Technology* 302 (2022): 122081, https://doi.org/10.1016/j.seppur.2022.122081.

56. S. Daliran, M. Ghazagh-Miri, A. R. Oveisi, et al., "A Pyridyltriazol Functionalized Zirconium Metal–Organic Framework for Selective and Highly Efficient Adsorption of Palladium," *ACS Applied Materials & Interfaces* 12 (2020): 25221–25232, https://doi.org/10.1021/acsami.0c06672.

57. X. Li, K. Zhang, G. Wang, et al., "Constructing Ambivalent Imidazopyridinium-Linked Covalent Organic Frameworks," *Nature Synthesis* 1 (2022): 382–392, https://doi.org/10.1038/s44160-022-00071-y.

58. Y. Gao, R.-Y. Zhou, L. Yao, et al., "Selective Capture of Pd(II) From Aqueous Media by Ion-imprinted Dendritic Mesoporous Silica Nanoparticles and Re-Utilization of the Spent Adsorbent for Suzuki Reaction in Water," *Journal of Hazardous Materials* 436 (2022): 129249, https://doi.org/10.1016/j.jhazmat.2022.129249.

59. G. Chen, Y. Wang, H. Weng, et al., "Selective Separation of Pd(II) on Pyridine-Functionalized Graphene Oxide Prepared by Radiation-Induced Simultaneous Grafting Polymerization and Reduction," *ACS Applied Materials & Interfaces* 11 (2019): 24560–24570, https://doi.org/10.1021/acsami.9b06162.

60. K. Zhang, Z. Chang, X. Luo, L. Yang, J. Pei, and S. Luo, "Specific Spatial Transfer $PdCl_4^{2-}$ to [X-Pd-Y] by Strong Coordination Interaction in a 3D Palladium Ion-Imprinted Polymer With Footprint Cavity," *Chemical Engineering Journal* 405 (2021): 126613, https://doi.org/10.1016/j.cej.2020.126613.

61. Y. Zhao, C. Xu, Q. Qi, et al., "Tailoring Delicate Pore Environment of 2D Covalent Organic Frameworks for Selective Palladium Recovery," *Chemical Engineering Journal* 446 (2022): 136823, https://doi.org/10.1016/j.cej.2022.136823.

62. Y. Wang, Y. Wu, J. Li, et al., "Ultra-Selective and Efficient Static/Dynamic Palladium Capture From Highly Acidic Solution With Robust Macrocycle-Based Polymers," *Advanced Functional Materials* 33 (2023): 2304051, https://doi.org/10.1002/adfm.202304051.

63. J. Purans, B. Fourest, C. Cannes, et al., "Structural Investigation of Pd(II) in Concentrated Nitric and Perchloric Acid Solutions by XAFS," *Journal of Physical Chemistry B* 109 (2005): 11074–11082, https://doi.org/10.1021/jp045489n.

64. L. Z. Zhong, Z. W. Yu, Q. Y. Zhang, X. F. Feng, and F. Luo, "Construction of Multiple-Component Covalent Organic Frameworks by an in Situ Approach for Boosting Palladium Recovery From Strong Acid," *ACS Materials Letters* 5 (2023): 2665–2672, https://doi.org/10.1021/acsmaterialslett.3c00876.

65. S. Jhulki, A. M. Evans, X.-L. Hao, et al., "Humidity Sensing Through Reversible Isomerization of a Covalent Organic Framework," *Journal of the American Chemical Society* 142 (2020): 783–791, https://doi.org/10.1021/jacs.9b08628.

66. Q. Zhu, L. Shi, Z. Li, G. Li, and X. Xu, "Protonation of an Imine-Linked Covalent Organic Framework for Efficient H_2O_2 Photosynthesis Under Visible Light up to 700 Nm," *Angewandte Chemie International Edition* 63 (2024): e202408041, https://doi.org/10.1002/anie.202408041.

67. G. Chen, L. Xu, C. Wang, et al., "Polyacid-Protonated Covalent Organic Frameworks Enable Stable and Efficient Photothermal Textiles," *Journal of the American Chemical Society* 148 (2026): 3148–3157, https://doi.org/10.1021/jacs.5c16049.

68. C. Xiang, Y. Wu, C. Shi, et al., "Process-Driven Protonation in Benzothiadiazole-Integrated Covalent Organic Frameworks: Activation of Peroxymonosulfate for Pollutant Oligomerization via Dominant Electron Transfer Process," *Angewandte Chemie International Edition* 65 (2026): e4772250, https://doi.org/10.1002/anie.4772250.

Supporting Information

Additional supporting information can be found online in the Supporting Information section.

Supporting File: The authors have cited additional references within the Supporting Information. Chemicals, instrumentation, experimental procedures, crystal data, and additional materials characterization data (FT-IR, crystal structures, SEM, TEM, PXRD, XPS, XAS measurements, adsorption calculations, and adsorption data).

15213773, 2026, 33, Downloaded from https://onlinelibrary.wiley.com/doi/10.1002/anie.202412007 by Shengqian Ma - University Of North Texas Willis Library , Wiley Online Library on [21/10/2026]. See the Terms and Conditions (https://onlinelibrary.wiley.com/terms-and-conditions) on Wiley Online Library for rules of use; OA articles are governed by the applicable Creative Commons License